# CCI

# BIOMASS

# END TO END ECV UNCERTAINTY BUDGET
# VERSION 5.0

| DOCUMENT REF: | CCI_BIOMASS_E3UB_V5 |
|---|---|
| DELIVERABLE REF: | D2.3-E3UB |
| VERSION: | 5.0 |
| CREATION DATE: | 2020-06-14 |
| LAST MODIFIED | 2023-11-30 |

## Document Authorship

| | NAME | FUNCTION | ORGANISATION | SIGNATURE | DATE |
|---|---|---|---|---|---|
| PREPARED | M. Santoro | | GAMMA | | |
| PREPARED | O. Cartus | | GAMMA | | |
| VERIFIED | H. Friendship-Kay | | Aberystwyth University | | |
| VERIFIED | R. Lucas | | Aberystwyth University | | |
| PREPARED | | | | | |
| PREPARED | | | | | |
| PREPARED | | | | | |
| PREPARED | | | | | |
| PREPARED | | | | | |
| PREPARED | | | | | |
| VERIFIED | S. Quegan | Science Leader | Sheffield University | | |
| APPROVED | | | | | |

## Document Distribution

| ORGANISATION | NAME | QUANTITY |
|---|---|---|
| ESA | Frank Seifert | |

## Document History

| VERSION | DATE | DESCRIPTION | APPROVED |
|---|---|---|---|
| 1.0 | 2019-02-27 | E3UB of CCI Biomass year 1 | |
| 2.0 | 2020-02-28 | E3UB of CCI Biomass year 2 | |
| 3.0 | 2021-06-14 | E3UB of CCI Biomass year 3 | |
| 4.0 | 2023-04-06 | E3UB of CCI Biomass year 4 | |
| 5.0 | 2023-11-30 | E3UB of CCI Biomass year 5 | |

## Document Change Record (from Year 1 to Year 4)

| VERSION | DATE | DESCRIPTION | APPROVED |
|---|---|---|---|
| 2.0 | 2020-02-28 | Updated the document to reflect changes in the ATBD of year 2 | |
| 3.0 | 2021-06-14 | Updated the document to reflect changes in the ATBD of year 3 | |
| 4.0 | 2023-04-06 | Updated the document to reflect changes in the ATBD of year 4 | |
| 5.0 | 2023-11-30 | Updated the document to reflect changes in the ATBD of year 5 | |

# Table of Contents

# LIST OF FIGURES

# SYMBOLS AND ACRONYMS

| | |
|---|---|
| ADP | Algorithm Development Plan |
| AGB | Above-ground Biomass |
| ALS | Airborne Laser Scanner |
| ASAR | Advanced Synthetic Aperture Radar |
| ATBD | Algorithm Theoretical Basis Document |
| BCEF | Biomass Conversion & Expansion Factor |
| BEF | Biomass Expansion Factor |
| CCI | Climate Change Initiative |
| CCI-Biomass | Climate Change Initiative – Biomass |
| DARD | Data Access Requirements Document |
| DEM | Digital Elevation Model |
| E3UB | End to End ECV Uncertainty Budget |
| ECV | Essential Climate Variables |
| ENL | Equivalent Number of Looks |
| ENVISAT | ESA Environmental Satellite |
| EO | Earth Observation |
| ESA | European Space Agency |
| FAO | Food and Agriculture Organization |
| FBD | Fine Beam Dual |
| GCOS | Global Climate Observing System |
| GEZ | Global Ecological Zones |
| GLAS | Geoscience Laser Altimeter System |
| ICESAT GLAS | Ice, Cloud, and land Elevation Satellite Geoscience Laser Altimeter System |
| JAXA | Japan Aerospace Exploration Agency |
| MPI-BGC | Max Planck Institute for Biogeochemistry |
| PSD | Product Specification Document |
| PVASR | Product Validation and Algorithm Selection Report |
| SAR | Synthetic Aperture Radar |
| URD | User Requirements Document |
| VCF | Vegetation Continuous Fields |

# REFERENCE DOCUMENTS

| ID | TITLE | ISSUE | DATE |
|---|---|---|---|
| RD-1 | Users Requirements Document | V3 | |
| RD-2 | Product Specification Document | V5 | |
| RD-3 | Algorithm Theoretical Basis Document | V5 | |
| RD-4 | Algorithm Development Plan | V5 | |
| RD-5 | Product Validation Plan (PVP) | V5 | |
| RD-6 | Product Validation Report (PVR) | V4 | |

# 1  Introduction

Above-ground biomass (AGB, units: Mg ha$^{-1}$) is defined by the Global Carbon Observing System (GCOS) as one of more than 50 Essential Climate Variables (ECV). For climate science communities, AGB is a pivotal variable of the Earth System, as it impacts the surface energy budget, the land surface water balance, the atmospheric concentration of greenhouse gases and a range of ecosystem services. The GCOS requirement is for AGB to be provided wall-to-wall over the entire globe for all major woody biomes at 500 m to 1 km spatial resolution with a relative error of less than 20% where AGB exceeds 50 Mg ha$^{-1}$ and a fixed error of 10 Mg ha$^{-1}$ where the AGB is below that limit.

One of the objectives of the Climate Change Initiative (CCI) Biomass project is to generate global maps of AGB using a variety of Earth Observation (EO) datasets using state-of-the-art models for several epochs and to assess biomass changes on both a yearly time scale and a decadal time scale. The maps should be spatially and temporally consistent; in addition, they need to be consistent with other data layers thematically similar to the AGB dataset produced in the framework of the CCI Programme (e.g., Fire, Land Cover, Snow etc.).

Algorithms to estimate AGB and its changes are described in the Algorithm Theoretical Basis Document (ATBD) [RD-3]. The scope of this document is to define and quantify the uncertainties associated with the biomass estimates. This End to End ECV Uncertainty Budget document (E3UB) relies on indications in the User Requirements Document (URD) [RD-1] and the Product Specifications Document (PSD) [RD-2]. Advances that may potentially be implemented in future revisions of the ATBD and in this document are described in the Algorithm Development Plan (ADP) [RD-4].

During Year 1 of the project, methods were developed that led to the generation of the global AGB product for the year 2017. In year 2, the methods were refined to generate a set of three global datasets of AGB for the years 2010, 2017 and 2018. In year 3, the AGB estimation methods have been refined towards an improved set of AGB maps, also allowing for an assessment of AGB changes between epochs. In year 4, the AGB and AGB change estimation methods evolved thanks to extensive spaceborne LiDAR measurements and access to JAXA's original L-band datasets. Annual maps of AGB were obtained for 2010 and 2017-2020 with corresponding AGB changes. In year 5, the CORE retrieval algorithm has been consolidated with additional satellite LiDAR and SAR datasets. The current data product of CCI Biomass consists of global AGB maps for 2010 and 2015-2021 with corresponding annual change maps and a decadal 2010-2020 change map.

Accordingly, with each iteration, the framework that quantifies the accuracy of each map has been updated. This report documents the framework adopted to quantify the precision of the AGB and AGB change estimates. The estimation of errors and biases is addressed in the Product Validation Plan [RD-5] and in the Product Validation Report [RD-6].

Section 2 provides the background of this E3UB, describing the strategy that underpins the algorithms implemented in CCI Biomass to estimate AGB and AGB change. Sections 3 and 4 describe the procedures implemented to characterize the precision of the AGB and the AGB change estimates, respectively.

# 2 Background

Accuracy describes how well the estimate of a certain quantity (e.g., AGB) matches its true value. For an ensemble of data, two gross statistical measures of the precision of the estimator are commonly used: bias, which is the expected value of the difference between the estimated and true value, and a quantity indicating the variability of the estimate (standard deviation). More complete descriptors could include, for example, confidence intervals on the estimates or the full error distribution. These descriptors are, however, practically impossible to obtain in our case because the errors of some of the parameters involved in the biomass retrieval scheme could only be assumed. A framework to estimate the bias of an AGB estimate is introduced in the ATBD of this project. The focus of this document is the characterization of the precision of the AGB and AGB change estimates starting from the standard deviation of the observations and the model parameters.

The precision of an AGB estimate from remote sensing data depends on the precision of the input data and the precision of the estimation procedure. Figure 2-1 shows the flowchart of the CCI Biomass CORE retrieval algorithm to generate annual global datasets of AGB estimates [RD-3].
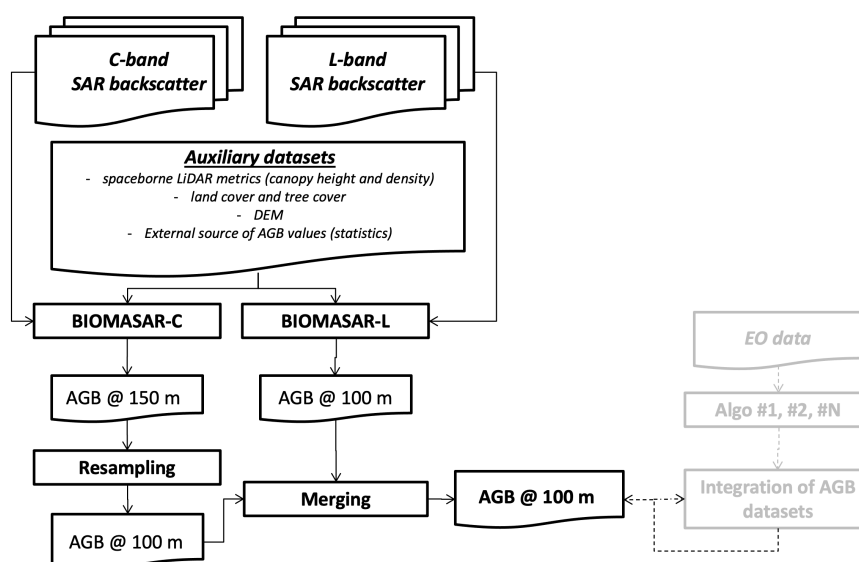


Figure 2-1: Functional dependencies of datasets and approaches forming the CCI Biomass CORE global biomass retrieval algorithm. The shaded part of the flowchart represents potential improvements following the implementation of additional retrieval techniques [RD-3].

The CORE algorithm foresees that two independent estimates of AGB are obtained from the BIOMASAR algorithm adapted to ingest C-band (BIOMASAR-C) and L-band SAR backscatter data (BIOMASAR-L). The AGB estimates are then combined to obtain a final estimate that should be characterized by smaller errors than the original values. Since the C- and L-band datasets have different pixel spacing, the AGB estimates from the BIOMASAR-C algorithm have slightly coarser resolution so are resampled to the geometry of the BIOMASAR-L estimates.

BIOMASAR-C and -L both rely on a model of the forest backscatter (Water Cloud Model) in which the SAR backscatter is related to canopy density and height. Two separate models expressing canopy density as a function of canopy height and canopy height as a function of AGB allow AGB to be directly

expressed in the forest backscatter model without having to rely on empirical coefficients, as is done in most parametric approaches aiming at estimating biomass.

The quantification of the standard deviation of an AGB estimate is described in Section 3 for each of the implementations, following the description of the algorithms in the ATBD.

AGB changes can be estimated either by differencing signals or by differencing estimates of AGB. The latter approach propagates errors of individual estimates but is the only viable solution if the framework to estimate changes considers multiple predictors, which furthermore have different characteristics (e.g., density of observations, sensor technical specifications). The synergy of spaceborne observations is the major strength of the CORE algorithm to obtain a reliable distribution of AGB estimates worldwide and implies that the AGB change products developed in this context rely on the individual maps rather than on the primary EO observations. The AGB change products are defined simply as the difference between maps between two epochs; here, we describe the quantification of the uncertainties, following the description of the AGB change product in the ATBD.

# 3 Methods to assign precision to AGB estimates

In this Section, we detail methods to quantify the standard deviation for each of the individual global inversion methods and for the final AGB product. First, we summarize the current implementation of the CCI Biomass CORE algorithm (Section 3.1). Then, the precision of the estimates from BIOMASAR-C and BIOMASAR-L are presented (Sections 3.2 and 3.3, respectively). The methods presented reflect our current understanding of the standard deviations embedded in the retrieval algorithms. For previous versions of the CORE retrieval algorithm and their uncertainty budget refer to the documents available at https://climate.esa.int/en/projects/biomass/key-documents/ (last access on 30 October 2023).

## 3.1 The modelling framework

The Water Cloud Model (WCM) with gaps, given as Equation (3-1), was derived from the original WCM presented by (Attema & Ulaby, 1978) to express the total forest backscatter of a forest as the sum of direct scattering from the ground through gaps in the canopy, ground scattering attenuated by the canopy and direct scattering from vegetation:

$$\sigma_{for}^0 = (1 - \eta)\sigma_{gr}^0 + \eta\sigma_{gr}^0 T_{tree} + \eta\sigma_{veg}^0(1 - T_{tree}) \tag{3-1}$$

Here $\eta$ is the area-fill or canopy density factor, representing the fraction of the area covered by vegetation, $\sigma^0_{gr}$ and $\sigma^0_{veg}$ represent the backscattering coefficients of the ground and vegetation layer, respectively, and $T_{tree}$ is the two-way tree transmissivity, which can be expressed as $e^{-\alpha h}$, where $\alpha$ is the two-way attenuation per meter through the tree canopy and $h$ is the depth of the attenuating layer.

Another formulation of the WCM relates the forest backscatter directly to the growing stock volume (GSV):

$$\sigma_{for}^0 = \sigma_{gr}^0 e^{-\beta V} + \sigma_{veg}^0\left(1 - e^{-\beta V}\right) \tag{3-2}$$

where β is an empirically defined coefficient expressed in ha m$^{-3}$ and expresses the forest transmissivity modelled as a simple exponential of the GSV, $V$.

By comparing Equations (3-1) and (3-2), the link between β, η and α is given by (Santoro et al., 2002):

$$e^{-\beta V} = 1 - \eta\left(1 - e^{-\alpha h}\right) \tag{3-3}$$

While Equation (3-3) can be considered valid in mature forests because height and GSV (or AGB) are almost linearly related, it is not correct throughout the entire range of biomass because of the non-linear relationship between the forest variables: canopy height, biomass, volume and canopy density.

Equation (3-2) was used in year 1 of CCI Biomass to estimate GSV. Starting with year 2, we considered the original WCM with gaps in Equation (3-1) and the set of functional dependencies between canopy density, tree height and above-ground biomass to express the WCM as a function of AGB [RD-3].

$$CD = 1 - e^{-qh} \tag{3-4}$$

$$AGB = p_1 h^{p_2} \tag{3-5}$$

The area-fill factor in Equation (3-1) can be assumed to correspond to canopy density in Equation (3-4).

The empirical coefficients $q$, $p_1$ and $p_2$ are regression coefficients estimated by means of non-linear least squares [RD-3]. The estimation of the parameter $q$ is currently supported by canopy density (CD) and height (h) derived from ICESat GLAS measurements of canopy density and top-of-canopy height (RH100). The estimation of the parameters $p_1$ and $p_2$ is currently supported by canopy height values derived from ICESat-2 measurements averaged at administrative or ecological unit level and corresponding AGB averages reported by National Forest Inventories (NFI) and based on forest field inventory measurements. The justification for using statistics instead of in situ measurements of AGB has been outlined in the ATBD [RD-3].

As we want to express the backscatter as a function of AGB, we first need to invert Equation (3-5), thus obtaining $h = (b_1 \cdot AGB)^{b_2}$ with $b_1 = 1/p_1$ and $b_2 = 1/p_2$. Equation (3-6) shows the forest backscatter (observable, $\sigma^0_{for}$) expressed as a function of AGB only

$$\sigma^0_{for} = \left[1 - \left(1 - e^{-q \cdot (b_1 \cdot AGB)^{b_2}}\right)\left(1 - e^{-\alpha \cdot (b_1 \cdot AGB)^{b_2}}\right)\right]\sigma^0_{gr}$$
$$+ \left(1 - e^{-q \cdot (b_1 \cdot AGB)^{b_2}}\right)\left(1 - e^{-\alpha \cdot (b_1 \cdot AGB)^{b_2}}\right)\sigma^0_{veg}$$

$$\tag{3-6}$$

In the remainder of this Section, we provide a description of the errors in the current retrieval method where AGB is directly estimated from the remote sensing data. The precision of AGB estimates derived from GSV estimates as done in year 1 is described in previous versions of this document available at https://climate.esa.int/en/projects/biomass/key-documents/ (last access on 30 October 2023).

The parameters $\sigma^0_{gr}$, $\sigma^0_{veg}$ and $\alpha$ are unknown a priori and need to be estimated. Their estimation is done in a slightly different manner depending whether the predictor consists of C- or L-band backscatter data.

In BIOMASAR-C, it is assumed that $\alpha$ remains constant and its uncertainty can be neglected because of its minimal impact on the retrieval. The estimates of $\sigma^0_{gr}$ and $\sigma^0_{veg}$ are obtained with a least squares regression of Equation (3-1) in which canopy height is expressed as function of canopy density derived from Equation (3-4). Expressing the WCM as a function of canopy density allows the estimation of the two unknown model parameters because the SAR backscatter can be related to values of canopy density derived from optical remote sensing images (e.g., Hansen et al, 2013). The estimate of $\sigma^0_{veg}$ from the regression is eventually corrected for with a compensation factor related to the fact that this estimate represents the backscatter of the densest forests and contains a fraction of the backscatter from the ground through gaps or attenuated by the canopy. This combined procedure, i.e., regression and compensation, is applied separately to each set of backscatter measurements and percent tree cover values characterized by a specific range of incidence angles.

For BIOMASAR-L, all three parameters need to be estimated. As for BIOMASAR-C, Equation (3-1) is regressed with three unknowns to observations of canopy density and SAR backscatter, using the allometry in Equation (3-4) to replace height with canopy density. The procedure is applied separately to each set of backscatter measurements and percent tree cover values characterized by a specific range of incidence angles.

Regardless of the BIOMASAR algorithm, the inversion of the WCM in Equation (3-6) to estimate AGB is done numerically for each SAR backscatter measurement at a given location. Given N observations of the SAR backscatter acquired within a predefined time interval (typically one year), the corresponding N estimates of AGB can be combined with a weighted average to form a new estimate of AGB. The resulting estimate will have higher precision than any of the individual AGB estimates but may not be closer to the true AGB if the estimates are biased.

$$AGB_{mt} = \frac{\sum_{i=1}^{N} w_i \widehat{AGB_i}}{\sum_{i=1}^{N} w_i} \tag{3-7}$$

The weights, $w_i$, in Equation (3-7) are defined as the vegetation-to-ground backscatter difference in dB, $\sigma^0_{veg} - \sigma^0_{gr}$, normalized by the maximum backscatter difference:

$$w_i = \frac{\sigma^0_{veg,i} - \sigma^0_{gr,i}}{max\left(\sigma^0_{veg,i} - \sigma^0_{gr,i}\right)} \tag{3-8}$$

Merging of the two BIOMASAR-C and BIOMASAR-L estimates of AGB is implemented in the form of a weighted average, where the weights account for three different calculated weights combined into one [RD-3]:

$$AGB = w(L)AGB_{mt,L} + w(C)AGB_{mt,C} \tag{3-9}$$

## 3.2  Quantifying the precision of the BIOMASAR-C estimates

### 3.2.1  Precision of the C-band backscatter measurements

The precision of a backscatter measurement is affected by the radiometric and calibration accuracies, thermal noise and speckle. The SAR pre-processing also introduces additional uncertainty related to: (i) the precision of the geocoding transformation and resampling between radar and map geometries; (ii) the horizontal and vertical precision of the Digital Elevation Model (DEM) used as reference for the map geometry, and (iii) the precision of the pixel area and local incidence angle used to normalize the

backscatter for slope-induced effects on the backscatter. Since the pixel-level uncertainties in the DEMs used in this study are unavailable, we cannot estimate the variance of a backscatter measurement from the individual variances of the terms listed above. We therefore estimate it empirically by equating it to the Equivalent Number of Looks (ENL).

In the ATBD [RD-3], our estimate of the ENL for a Sentinel-1 observation was 162 (median value) with a span of [90, 375] but most values lie between 100 and 250. Assuming a constant ENL of 162 for Sentinel-1, we obtain a standard deviation of 0.32 dB. In the ATBD, we also presented the ENL for monthly averages of the Sentinel-1 backscatter. Because of the high temporal correlation within a month, the Sentinel-1 dataset can be reduced in size substantially without impacting the AGB estimation. The ENL of 150 characterizing monthly averages corresponds to a standard deviation of 0.34 dB.

In Santoro et al. (2015), we quantified the standard deviation of Envisat ASAR backscatter observations as a function of the number of observations available in the multi-channel speckle filter: 0.6 dB for N ≤ 50; 0.5 dB for 51 ≤ N ≤ 150; and 0.4 dB for N > 150, where N is the number of backscatter observations at a pixel.

These values are here used to characterize the $\delta\sigma^0_{meas}$ component of the standard deviation of the biomass estimates (see Equation (3-12) in Section 3.2.2).

### 3.2.2 Precision of AGB from a backscatter observation

The precision of an AGB estimate obtained from a single observation of the SAR backscatter is quantified by propagating the standard deviation of (i) the measured SAR backscatter, $\sigma^0_{meas}$, (ii) the estimates of the forest backscatter model parameters $\sigma^0_{gr}$ and $\sigma^0_{veg}$, (iii) the coefficient of the model relating canopy density and RH100, $q$, and (iv) the coefficients of the model relating canopy height and AGB, $p_1$ and $p_2$.

The estimates of $\sigma^0_{gr}$ and $\sigma^0_{veg}$ are first obtained by least squares regression to the model in Equation (3-1) expressed in terms of canopy density only, for 10° wide intervals of local incidence angle. Then, a quadratic function is established to describe the variation of each parameter as a function of incidence angle [RD-3]. Accordingly, the standard deviations of $\sigma^0_{gr}$ and $\sigma^0_{veg}$ are obtained from the variance-covariance matrix for the fitted coefficients using Equation (3-1). The covariance term was usually much smaller than the variance terms, thus confirming the assumption that the two parameters are independent of each other. Then, the standard deviations of $\sigma^0_{gr}$ and $\sigma^0_{veg}$ per incidence angle range are transformed with the error model of the quadratic function to obtain a value for each incidence angle. The error propagation is programmed in the polyconf tool of the Matlab scripting language.

The standard error of the coefficient $q$ was calculated through bootstrapping with replacement for each of the ecoregions, with 100 iterations per ecoregion. Figure 3-1 shows the spatially explicit map of the standard error of $q$ obtained by interpolating the individual value per ecoregion with bicubic interpolation to avoid offsets at the boundary of ecoregions. The standard error ranged from 0 to 143%, although it was highly correlated with the number of available footprints per ecoregion (Figure 3-2), with ecoregions with more than 100 footprints all having a relative standard error < 10%. Larger errors were obtained for ecoregions characterized by sparse to almost absent forest cover, in which case the number of GLAS footprints used to estimate $q$ was small.

The standard deviation of the coefficients $p_1$ and $p_2$ was obtained from the confidence intervals estimated when fitting sub-national averages of AGB from the NFI and Forest Resources Assessment (FRA) statistics and the corresponding averages of canopy height from the spaceborne LiDAR datasets [RD-3].

Figure 3-3 shows that the standard deviation of the coefficient $p_1$ varied spatially, being below 20% of the estimated value except for the United States where the values were larger than 100%. The standard deviation of the coefficient $p_2$ was less uncertain, being mostly 10% of the estimated value and always below 20%.
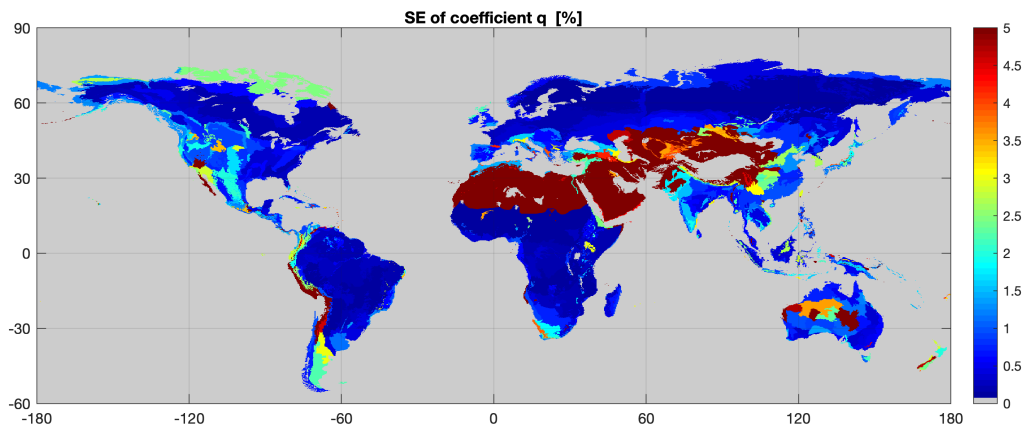


Figure 3-1: Spatially interpolated maps of the standard error of the coefficient q. The map shows the standard error relative to the estimate of each parameter.
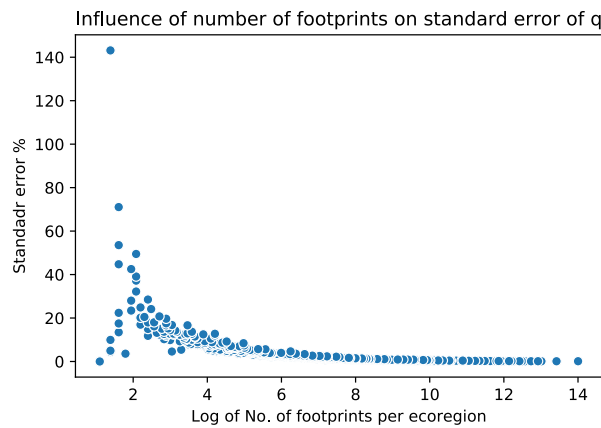


Figure 3-2: Scatterplot demonstrating the influence of the number of available ICESat GLAS footprints within an ecoregion on the standard error of the q value obtained
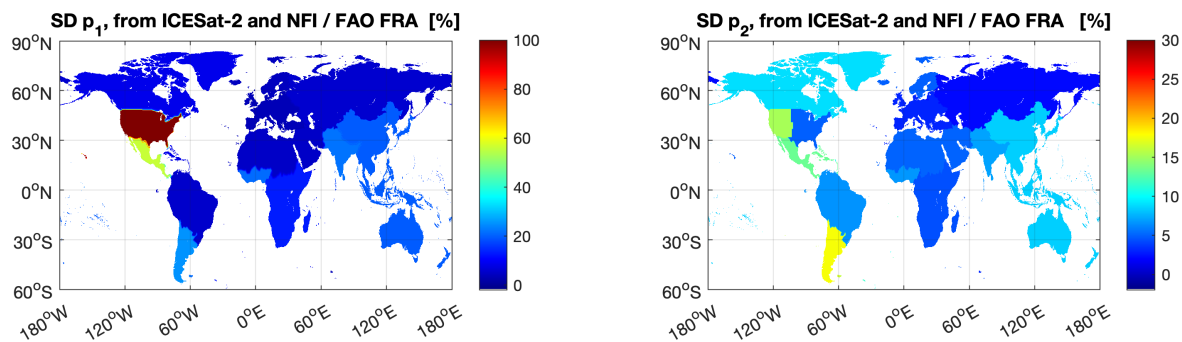
Figure 3-3: Maps of the relative standard deviation of coefficients $p_1$ and $p_2$, i.e. the ratio between the standard deviation and the estimate of each coefficient. Maps of the two coefficients are displayed in [RD-3].

Because of the numerical inversion to estimate AGB from a backscatter observation, the computation of the standard deviation of an AGB estimate needs to be handled with a numerical approach. This means that the retrieval model parameters involved in the estimation of the AGB ($\sigma^0_{meas}$, $\sigma^0_{gr}$, $\sigma^0_{veg}$, $q$, $p_1$ and $p_2$) are perturbed on the basis of their individual standard deviations and a perturbed AGB is estimated. This procedure is repeated N times for each pixel and in each SAR image to create, for each time, a vector of perturbed AGB estimates from which the standard deviation corresponding to a retrieved AGB at a given pixel and image is computed.

### 3.2.3 Precision of the multi-temporal AGB estimate

The multi-temporal AGB estimate is obtained as a linear combination of AGB estimates from images acquired at different times, with different polarizations and look angles, in order to reduce the noise affecting the individual estimates of AGB. Accordingly, the standard deviation of the multi-temporal estimate of AGB is obtained from a weighted average.

If the backscatter observations were independent, the standard deviation of the final AGB estimate would correspond to the square root of the weighted sum of the variances of each individual AGB estimate. In reality, observations are correlated, so the variance of the multi-temporal AGB estimates is the sum of a variance component and a covariance component that accounts for the correlation between errors.

$$\delta(AGB_{mt})^2 = \sum_{i=1}^{N} w_i^2\, \delta(AGB_i)^2 + 2 \sum_{i=1}^{N-1} \sum_{j=i+1}^{N} w_i\, w_j\, Cov(AGB_i, AGB_j) \qquad (3\text{-}10)$$

where

$$Cov(AGB_i, AGB_j) = \delta AGB_i \delta AGB_j r_{ij} \qquad (3\text{-}11)$$

The variance component is modelled as a linear combination of the single-image AGB variances. Here, it is assumed that the multi-temporal weights are the best estimates of the individual variances of the individual estimates of AGB. The covariance component is expressed in a similar manner where individual error covariances are weighted. The symbol $r_{ij}$ represents the correlation of errors between the estimates of AGB from image i and image j.

Computing the correlation of errors requires a reference dataset. The only viable solution is to use maps of AGB, since plot measurements are typically too sparse to allow a spatially explicit characterization of the error covariance. Airborne laser-based maps of AGB are the most suitable reference dataset for characterizing the error covariance. Although such maps are not free from errors, it is reasonable to assume that their impact on the correlation of errors is minimal because of their normal high precision. Obviously, maps lacking complete characterization of errors and with low precision should be discarded, which poses a serious issue when attempting to generate wall-to-wall values of the error covariance. In our assessment of the temporal correlation of errors, we used LiDAR-based AGB generated within CCI Biomass from airborne datasets over sites distributed across the U.S., the Brazilian Amazon, Kalimantan and Australia. The methodology is described in Labriere et al. (2018).

Because of the different characteristics of the Sentinel-1 and the Envisat ASAR datasets used to estimate AGB with BIOMASAR-C, we assessed their error correlations separately.

### 3.2.3.1 Sentinel-1

Figure 3-4 shows a matrix reporting at each bin the correlation of the errors between AGBs derived from Sentinel-1 images i and j using as a reference the LiDAR-based AGB from the CHEQ site part of the National Ecological Observatory Network (NEON) in the U.S. Both Sentinel-1 and LiDAR data were acquired in 2017. The index on each axis represents the sequential index of each monthly backscatter average covering the site (i.e., 1, 2, 3 etc. mean first, second, third, etc. average image in 2017). Odd integers refer to VH-polarized images. Even integers refer to VV-polarized images. The correlation matrix shows several blocks, each corresponding to a set of 24 images (i.e., 12 months and 2 polarizations) from a given orbital track covering the site. Empty blocks imply that the two orbital tracks being correlated did not have any overlap. For this particular site, the correlation was moderate for images acquired along the same orbital track (blocks along the main diagonal), regardless of the month of acquisition of the images. The correlation was also moderate in off-diagonal blocks corresponding to adjacent orbital tracks; also in this case, the correlation did not show any temporal dependency. However, the correlation was close to zero when it was computed for images acquired along two different orbital directions.
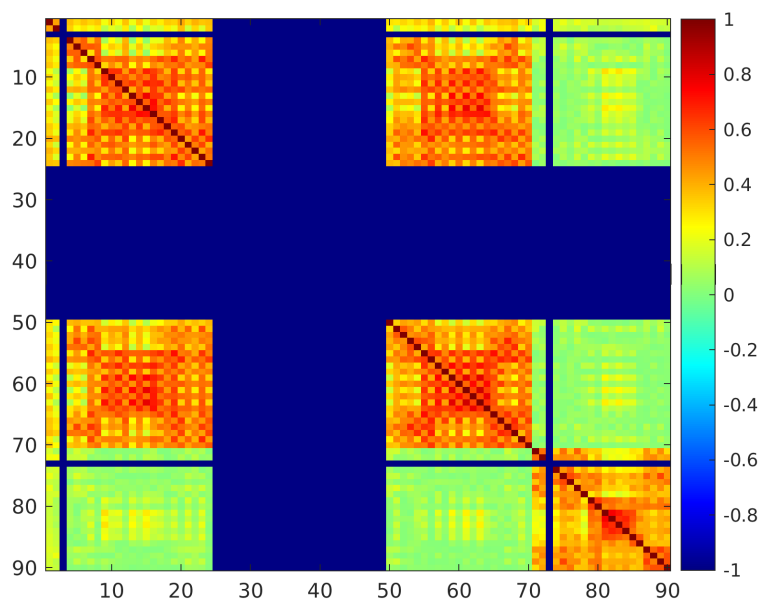
Figure 3-4: Matrix of error correlations for Sentinel-1 AGB estimates for the NEON CHEQ site in the U.S. located at 90°W, 45°N.

To assess whether the error correlation exhibited any temporal dependency, we created scatterplots reporting the error correlation as a function of the temporal lag between the first and the second AGB estimate, i.e., Sentinel-1 monthly average. In Figure 3-5, we include an example from one site per region. The numbers on the horizontal axis refer to the month of acquisition of the second Sentinel-1 image and the correlation refers to the error correlation coefficient with respect to the first month of 2017. The examples show moderate to weak sensitivity of the correlation to the temporal lag. The sensitivity was more prominent for sites with overall low AGB. Also the range of correlation values differed from site to site, depending on the AGB level.

To obtain a general impression of possible dependencies of the correlation coefficient on the AGB level, we computed the average correlation coefficient for each site and plotted it as a function of the average AGB per site (**Error! Reference source not found.**). We split the assessment per polarization, resulting in three possible combinations. There is no apparent dependency of the correlation coefficient on AGB or polarization.

Figure 3-5: Temporal distribution of error correlation of AGB estimates from the Sentinel-1 monthly averages for one site within each of the four regions covered by airborne LiDAR datasets. In each panel, we report the average AGB from the LiDAR-based map.
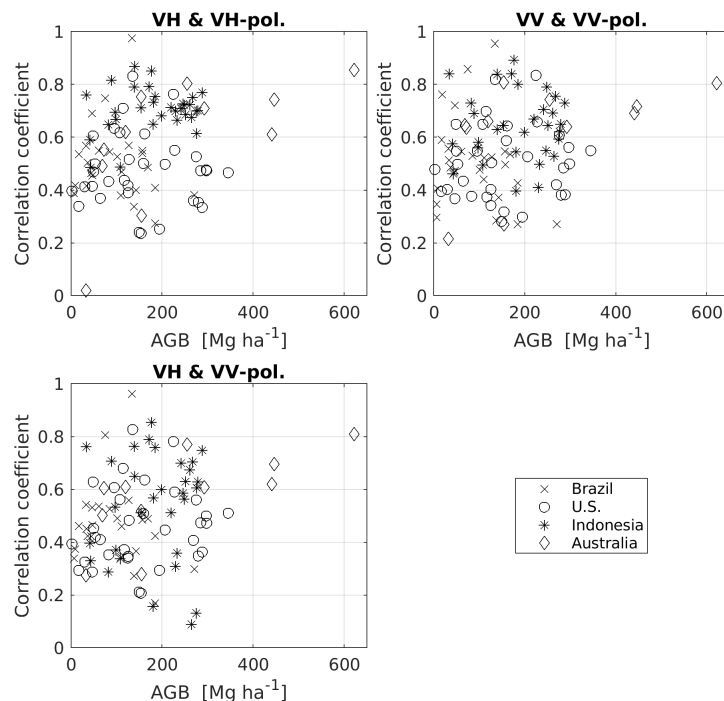


Figure 3-6: Scatterplots comparing the average error correlation per site with the LiDAR-based AGB average. Data points were split depending on the polarization of the first and the second Sentinel-1 image.

Although the LiDAR-based datasets included a wide variety of forest types and structural conditions, the scatter in each of the panels in **Error! Reference source not found.** was large, from which we conclude that there is no obvious driver of the error correlation in time. Hence, in the first instance, we used a simple generic value, such as the median of all correlations, to represent the correlation of AGB errors in time. The median value was 0.52.

The total standard deviation and its components in Equation (3-10) are illustrated in Figure 3-7 for a 1° x 1° tile in Tanzania (lower panels). We also include the map of AGB and an image showing the number of Sentinel-1 monthly average backscatter observations used to retrieve AGB (upper panels). It is notable that, at this stage, AGB has been retrieved regardless of the land cover (i.e., values of AGB have also been associated with water bodies and cropland). These areas need to be masked out for any further analysis of the data. Because of the large number of observations used to retrieve AGB, the variance term of the AGB standard deviation becomes small. The covariance term instead is large because of the moderate value used for the temporal correlation of errors. Figure 3-7 indeed indicates that the AGB standard deviation is driven by the error covariance component.
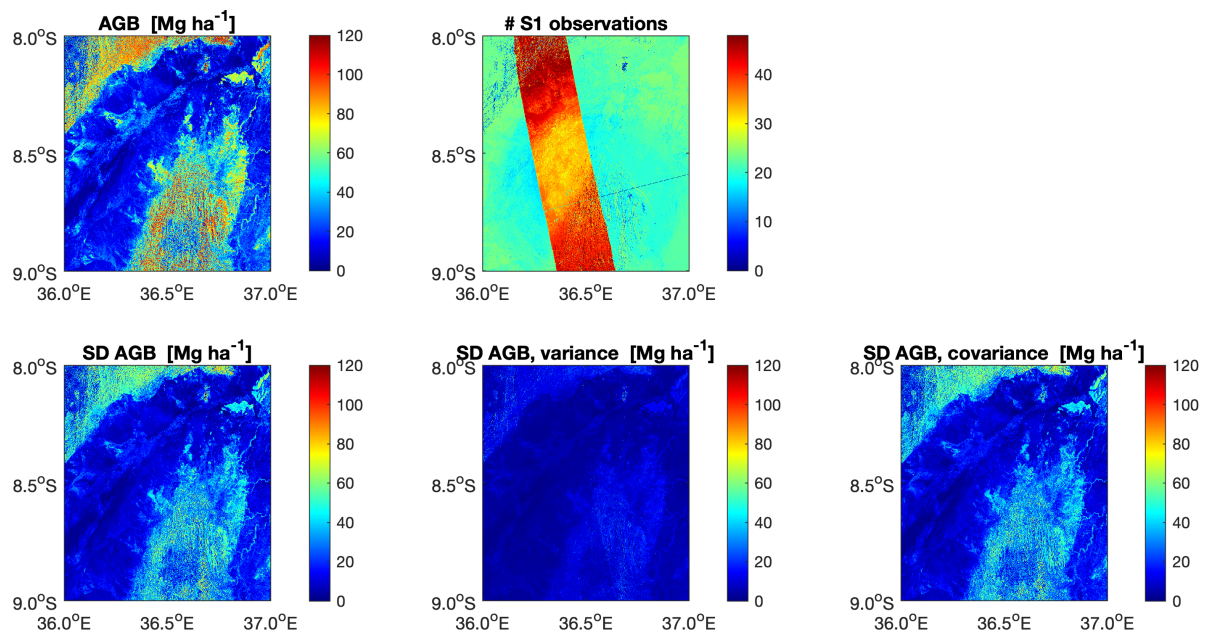


Figure 3-7: Maps of AGB, number of Sentinel-1 observations (monthly averages) and AGB standard deviations for a one degree tile. For the AGB standard deviation (SD), the variance and the covariance component are also displayed.

### 3.2.3.2   Envisat ASAR

This Section presents the same types of plots and diagrams for Envisat ASAR. Figure 3-8 shows the matrix of correlation between AGB estimation errors for all pairs of images over the NEON site considered for the Sentinel-1 analysis. The correlation was moderate to high only for two images close in time, i.e., for data points close to the main diagonal, or for two images acquired along the same orbital track. Away from the main diagonal, i.e., for longer time intervals, the correlation was low, without apparent seasonal effects.
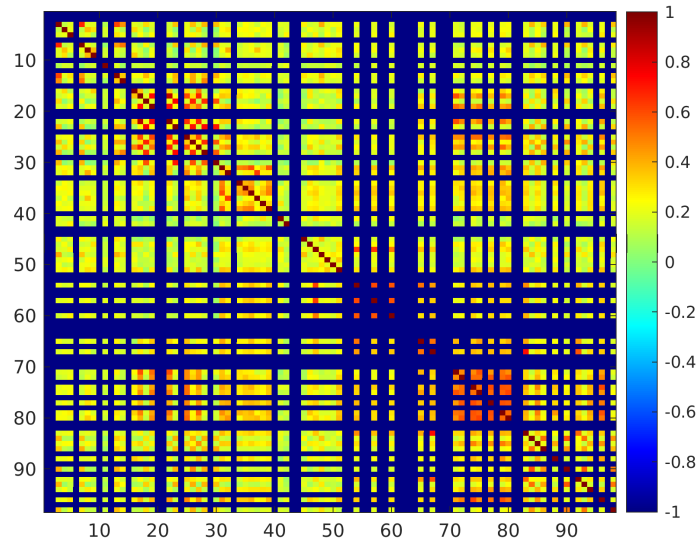
Figure 3-8: Matrix of error correlations for ASAR AGB estimates for the NEON CHEQ site in the U.S. located at 90°W, 45°N.

To assess the dependency of the error correlation on the time lag between image acquisitions, we show in Figure 3-9, correlation values for each pair of images aggregated by a lag expressed in months. There is no clear effect of the temporal interval on the correlation but we observe different levels of correlation depending on the region where the airborne LiDAR data used as reference was collected. Compared to Sentinel-1, the results are more varied because we estimated AGB from individual images rather than from monthly averages. In addition, the ASAR datasets always consisted of a small number of images (between 5 and 50) over the regions from which the airborne LiDAR data were available. This is probably a limitation to the interpretation of the error correlation signatures.
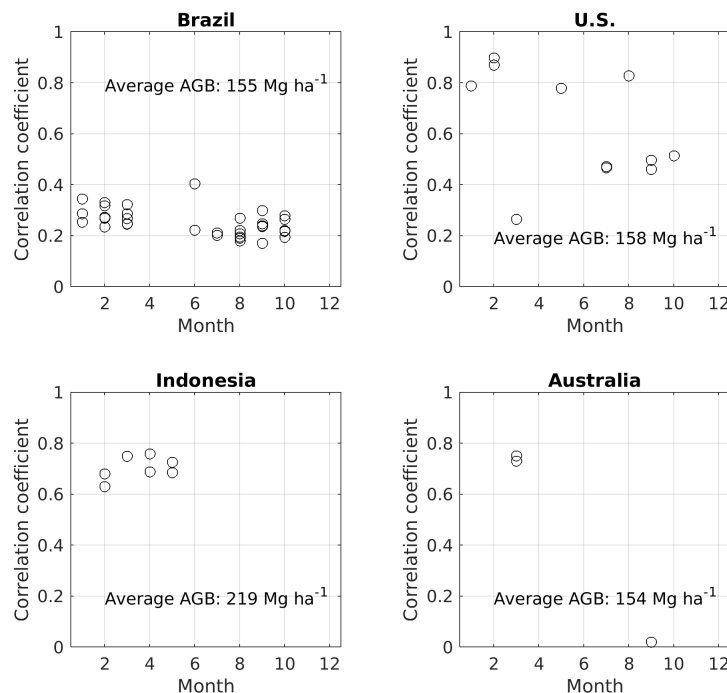


Figure 3-9: Temporal distribution of error correlation for AGB estimates derived from Envisat ASAR data for one site within each of the four regions covered by airborne LiDAR datasets. In each panel, we report the average AGB from the LiDAR-based map.

In Figure 3-10, we display the average error correlation values for each site and region, grouped by polarization type, as a function of average AGB per site. As for the Sentinel-1 analysis, we did not identify any dependency of the error correlation on polarization or AGB. The very large spread of values suggests that there may be other reasons explaining the level of correlation; however, as we could not identify any such dependency with the data available, we adopted a single global value for the error correlation in our computations. This was set to the average of all correlation values, i.e., 0.42. Because of the moderate error correlation, the standard deviation of the AGB estimates from the ASAR data contained a covariance component much larger than the variance component.
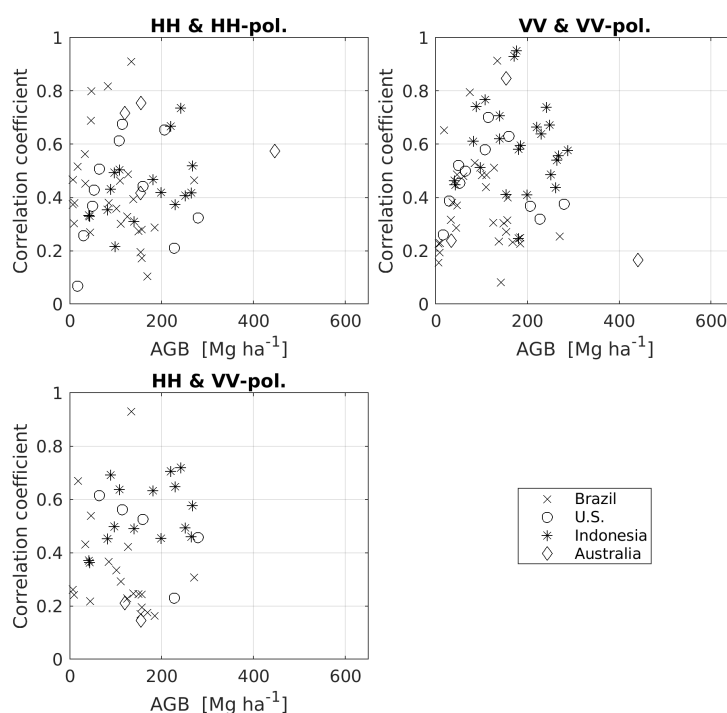


Figure 3-10: Scatterplots comparing the average error correlation per site with the LiDAR-based AGB average. Data points were split depending on the polarization of the first and the second ASAR image.

## 3.3  Quantifying the precision of the BIOMASAR-L estimates

### 3.3.1  Accuracy of the L-band backscatter measurements

The ALOS-1 PALSAR-1 and ALOS-2 PALSAR-2 FBD and ScanSAR datasets introduce errors in the AGB retrieval  associated with speckle, thermal noise, and errors in calibration, geocoding, and topographic corrections. In previous versions of the ATBD [RD-3], we documented radiometric and geometric errors of the datasets processed by JAXA to radiometric terrain-corrected level that were presumed due to the fact that the ALOS PRISM DEM had not been compensated for elevation offsets between the geoid (DEM reports geoid referenced heights) and the WGS84 ellipsoid locally. This resulted in systematic geolocation errors of the backscatter imagery of up to several pixels, depending on the Geoid-WGS84 elevation offset. In addition, the ALOS PRISM DEM used by JAXA in the processing presented artifacts which resulted in artifacts in the backscatter imagery, locally.

For the production of version 4 of the CCI Biomass AGB maps, we were able to use an entirely reprocessed database of ALOS-1 PALSAR-1 and ALOS-2 PALSAR-2 images.  JAXA reprocessed the per-

cycle mosaics of the ALOS-2 PALSAR-2 ScanSAR imagery with an updated version of the ALOS PRISM DEM to correct for the systematic geolocational errors observed in previous releases of the dataset as well as local errors associated with artifacts in the DEM. The ALOS-2 PALSAR-2 FBD imagery, instead, was now provided by JAXA in the form of detected images in slant-range geometry which were processed to radiometric terrain-corrected level by the CCI Biomass consortium using the 1 arcsec Copernicus DEM. In the case of the ALOS-1 PALSAR-1 FBD imagery, we now use the recently released backscatter images in Level 2.2 (L2.2) format for which images had been processed by JAXA to radiometric terrain-corrected level at 12.5 m resolution in UTM projection. In contrast to the ALOS-1 FBD mosaics that had to be used for production of the 2010 AGB map in previous releases of the CCI Biomass datasets, the Level 2.2 imagery  i) includes all individual  observations of the backscatter at HH and HV polarizations, and ii) presents improved geolocational accuracy. Evaluation of the new ALOS-2 FBD and ScanSAR datasets confirmed the high geolocational accuracy with errors in the range of few metres. In the case of the ALOS-1 L2.2 FBD imagery, we still find geolocational errors of the order of about a pixel, i.e., 12.5 metres. Nonetheless, after reprojection of the dataset to the target pixel grid in geographic coordinate system with a resolution of 0.00088888°, we find the accuracy of the L2.2 imagery superior to the accuracy of the annual FBD mosaics used in previous releases.

The ENL of the imagery was assessed for a number of homogenous forest patches, identified by means of visual image interpretation. We find the ENL of the backscatter at 0.00088888° resolution to be 80 or higher across the imagery acquired by ALOS-1 PALSAR-1 and ALOS-2 PALSAR-2 in FBD and ScanSAR modes and thus high enough to support multi-temporal AGB retrieval (which further reduces the influence of speckle noise) without applying additional speckle filtering.

### 3.3.2   BIOMASAR-L for AGB retrieval

As for C-band, the precision of AGB estimates derived from single L-band backscatter observations is quantified by propagating the standard deviations of backscatter measurements, estimates for the model parameters $\sigma^0_{gr}$ and $\sigma^0_{veg}$, the coefficient relating canopy density and height, and the coefficients of the allometry relating canopy height to AGB. In the error propagation, we also propagate errors associated with the two-way signal attenuation coefficient. So far only very few measurements of the attenuation have been published. We here assume a standard deviation of 0.25 dB/m, which is roughly consistent with the range of values reported in the literature (Ulaby et al., 1990; Chauhan et al., 1991; Shinohara et al., 1992; Sheen et al., 1994; Kurum et al., 2009; Praks et al., 2012).

In order to characterize the error correlation between AGB estimates derived from individual backscatter observations, we used airborne laser scanner (ALS) derived estimates of AGB as reference. Figure 3-11 exemplifies the error correlation for several forest sites located in the tropical, sub-tropical, temperate, and boreal zones. In the left column of the figure, error correlations are presented for the ALOS-1 PALSAR-1 FBD imagery acquired in 2010. In the second column, error correlations are presented for the imagery acquired in 2018 by ALOS-2 PALSAR-2 in FBD and ScanSAR modes. In general, we find that retrieval errors are significantly correlated at all sites with an average Pearson correlation coefficient of the order of 0.5.  While we expect significant deviations locally dependent on seasonal variations of the imaging conditions, repeat intervals of image acquisitions, technical specifications of the acquisition mode (e.g., FBD vs. ScanSAR), etc., the data sets at hand (i.e., sparse coverage of ALS derived AGB maps and L-band backscatter observations in most areas not covering all seasons) at this point do not permit a more systematic global analysis of the different factors influencing the correlation of errors. We therefore assume a constant error correlation of 0.5.
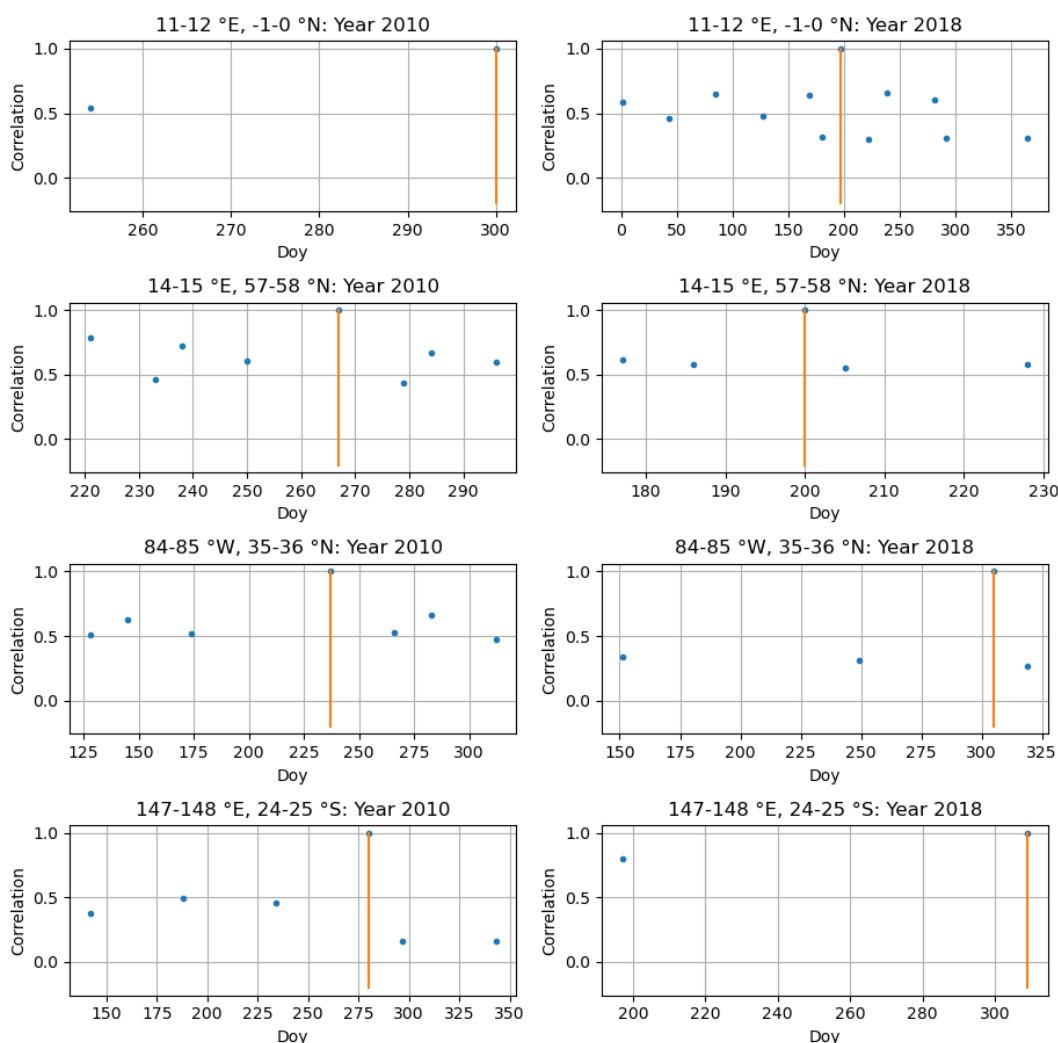
Figure 3-11: Correlation of AGB retrieval errors for a multi-temporal stack of L-band images acquired over different regions. The vertical line denotes the reference image against which the correlation of retrieval errors with respect to the other available images was assessed.

## 3.4 Quantifying the precision of the merged biomass estimates

When combining estimates from BIOMASAR-C and BIOMASAR-L, Equation (3-14) can be used to calculate the standard deviation of the merged product starting from the standard deviations of the BIOMASAR-C and BIOMASAR-L estimates.

$$\delta(AGB)^2 = w^2(L)\delta(AGB_{mt,L})^2 + w^2(C)\delta(AGB_{mt,C})^2 \qquad (3\text{-}14)$$

# 4 Methods to assign precision to AGB spatial averages

The CCI Biomass AGB datasets contain global estimates of AGB and AGB standard deviation in Mg/ha. The AGB dataset is provided in the geographic map projection, with a pixel size of 0.000888888° in latitude and longitude, corresponding approximately to 1 ha at the Equator. By averaging AGB estimates over neighbouring pixels, it is possible to generate aggregated AGB data products

representing biomass at coarser spatial scales. If the AGB values were independent, the variance of the average AGB, $\delta(AGB_{ave})^2$, would correspond to the sum of the individual AGB variances (i.e., squared AGB standard deviation, $\delta(AGB_i)^2$ ) divided by the number of pixels, N, within the averaging window

$$\delta(AGB_{ave})^2 = \frac{1}{N} \cdot \sum_{i=1}^{N} \delta(AGB_i)^2 \tag{3-15}$$

The variance and the standard deviation of the average AGB, $SD_{AGB_{ave}}$, are related as follows:

$$SD_{AGB_{ave}} = \sqrt{\delta(AGB_{ave})^2} \tag{3-16}$$

In reality, spatial autocorrelation cannot be neglected, so the standard deviation of the average AGB also needs to take into account an error covariance component that accounts for the spatial correlation of AGB errors.

$$\delta(AGB_{ave})^2 = \frac{1}{N} \cdot \sum_{i=1}^{N} \delta(AGB_i)^2 + \frac{2}{N} \cdot \sum_{i=1}^{N-1} \sum_{j=i+1}^{N} Cov(\delta AGB_i, \delta AGB_j) \tag{3-17}$$

where

$$Cov(\delta AGB_i, \delta AGB_j) = r_{spat,ij} \cdot \delta AGB_i \cdot \delta AGB_j \tag{3-18}$$

The symbol $r_{spat,\,ij}$ represents the correlation of errors between the estimates of AGB from pixel *i* and pixel *j* within the averaging window.

Computing the correlation of errors requires a reference dataset of AGB. In the case of wall-to-wall estimates, the only viable solution is to use maps of AGB as a reference since plot measurements are typically too sparse and unevenly distributed to allow a spatially explicit characterization of the spatial error covariance. Instead, ALS-based maps of AGB are a viable reference dataset. Although such maps may be biased, such biases are neglected here. The assumed lack of bias is supported by the fact that such maps are often produced at high resolution although here they are used in the form of averages at 1 hectare scale.

A major factor limiting the use of ALS maps of AGB is that there are only a few for which the error structure has been reported. Knowledge of the error structure is fundamental to deciding whether to select an AGB LiDAR dataset as reference. Also relevant is that the maps should cover an area sufficiently large to identify spatial autocorrelation patterns.

At the time of compiling this document, we identified the set of LiDAR-based AGB maps listed in Table 4-1 to characterize the AGB error covariance. The datasets represented all major forest ecotones to aid understanding of potential spatial patterns in the AGB error correlation. However, this set of LiDAR AGB maps cannot be considered representative for global forests, so the values derived from them need to be interpreted as plausible assumptions on error correlation.

Table 4-1: Sites used in this study to characterize the AGB error correlation

| Title | Region/site | Year | Ecozone | Reference |
|---|---|---|---|---|
| Forest base map (12. 5m) | Sweden | 2009-2014 | Boreal | https://www.skogsstyrelsen.se/skogligagrunddata<br><br>(Nilsson et al., 2017)<br>(last access on 30 January 2023) |
| CMS Biomass (20 m) | Sonoma County, California | 2013 | Temperate and sub-tropical | https://daac.ornl.gov/CMS/guides/CMS_LiDAR_Biomass_CanHt_Sonoma.html<br><br>(Dubayah et al., 2017) |
| ESA TROPISAR (25 m) | Nouragues and Paracou, French Guyana | 2009 | Tropical | https://earth.esa.int/web/guest/campaigns<br><br>(Labriere et al.., 2018) |
| ESA AfriSAR (25 m) | Lope, Gabon | 2013 | Tropical forest savannah mosaic | https://earth.esa.int/web/guest/campaigns<br><br>(Labriere et al., 2018) |
| NEON (100 m) | U.S. | 2017 | Temperate and subtropical | https://data.neonscience.org/home<br>(last access on 30 January 2023)<br><br>(data prepared by N. Labrière and J. Chave) |
| CMS Kalimantan (100 m) | U.S. | 2014 | Tropical | https://daac.ornl.gov/CMS/guides/CMS_LiDAR_Indonesia.html<br>(last access on 30 January 2023)<br><br>(data prepared by N. Labrière and J. Chave) |
| SLB Brazil (100 m) | Brazil | 2014-2018 | Tropical | https://www.paisagenslidar.cnptia.embrapa.br/webgis/<br>(last access on 30 January 2023)<br><br>(data prepared by N. Labrière and J. Chave) |
| TERN (100 m) | Australia | 2015-2018 | Tropical | https://www.tern.org.au/tern-observatory/landscape-monitoring-and-observation/<br>(last access on 30 January 2023)<br><br>(data prepared by N. Labrière and J. Chave) |

The LiDAR maps were tiled according to the predefined 1° x 1° grid used for the CCI Biomass maps. For each grid cell, we computed the semi-variogram of the AGB residuals, i.e., of the difference between map AGB and LiDAR AGB at 100 m. In total, we computed semi-variograms in 142 grid cells. An empirical exponential function relating the empirical semi-variogram to the lag distance in Equation (3-19) was then fitted to each semi-variogram. This function was found to be robust in terms of model fit to the observations and performed slightly better than the rise-to-the-max semi-variogram fit proposed by Mc Roberts et al., 2006.

$$v = n \cdot e^{-b \cdot D} + s \cdot \left(1 - e^{-b \cdot D}\right) \tag{3-19}$$

In Equation (3-19), $v$ represents the fitted semi-variogram, $n$ the nugget, $s$ the sill, $D$ the lag distance and $b$ is an empirical coefficient.

The fitted semi-variogram was finally expressed in terms of a correlation coefficient as in Equation (3-20). The function was normalized by the difference between the sill and the nugget to account for the fact that the error correlation should be 1 for a lag of 0 pixels.

$$r = 1 - \left(\frac{v-n}{s-n}\right) \tag{3-20}$$

To obtain a direct functional dependence between the lag (in pixels) and the correlation coefficient, Equations (3-19) and (3-20) can be nested and rewritten in a single Equation

$$r = 1 - e^{-k \cdot D} \tag{3-21}$$

Figure 4-1 shows an example of an empirical and fitted semi-variograms for the CMS Sonoma County dataset. For a lag of approximately 100 pixels, corresponding to 10 km, the model describing the semi-variogram approached a plateau, indicating that for larger distances AGB samples can be considered independent. The plot on the right-hand side of Figure 4-1 shows Equation (3-21) relating the error correlation to the lag distance (in pixels).
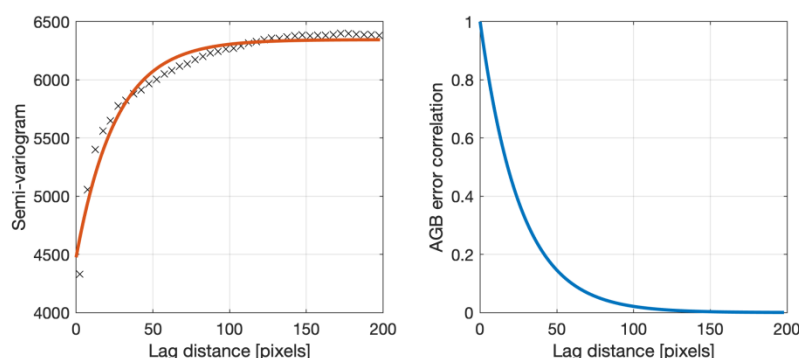


Figure 4-1: Empirical and fitted semi-variograms for the Sonoma County dataset described in Table 4-1 (left) and modelled AGB error correlation as a function of lag distance (right).

Figure 4-2 shows the ensemble of all fitted Equations (3-21) represented by the 10th and 90th percentiles of predicted error correlation for each lag distance between 0 and 500 pixels, i.e., up to 50 km. Most models predicted a rapid decrease of the error correlation, which became almost negligible for distances larger than 100 pixels (i.e., 10 km). Given the small extent of most LiDAR maps (all except for the country-wide dataset of Sweden), it was not possible to draw any conclusion about spatial patterns of the AGB error spatial autocorrelation. For this reason, it was decided to implement a single, global model for the error covariance, which corresponded to the ensemble average of all models created with the available reference AGB datasets. The ensemble average model is shown in Figure 4-2 by the thick curve. The ensemble average was characterized by a rather rapid decay of correlation for increasing lag distance; at about 200 pixels distance, the correlation was practically negligible.
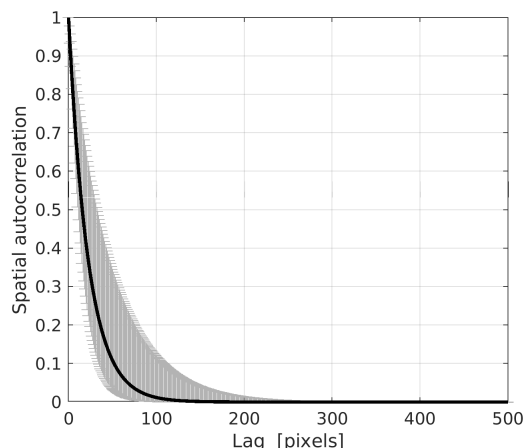
Figure 4-2: Model fits of Equation (3-21) for sites listed in Table 4-1. For the ensemble model, the coefficient *k* was estimated to be 0.0445.

In the absence of sufficient data, , the spatial variability of the AGB error correlation is neglected in our "global" ensemble model. This deficiency may be significant if the AGB error structure in some regions is not represented by the sites listed in Table 4-1. Hence more complete characterization of the AGB error structure is needed in the future; ALS-based maps as well as dense observations by currently operating laser systems in space (GEDI and ICESAT-2) are key to expanding knowledge in this direction.

Equation (3-17) requires that the error correlation for each pair of pixels in the averaging window is computed. Following the modelling framework proposed above, this is equivalent to computing the distance between each pair of pixels and estimating the error correlation from Equation (3-21). This can be computationally intensive, especially for large averaging windows. For a M×M averaging window, (N*(N-1))/2 correlations need to be computed, M being the number of pixels selected within the averaging window (N ≤ M*M). For a target resolution of 0.5° (M = 562), this would correspond to $5 \times 10^{10}$ computations if all pixels were been selected.

To propagate the uncertainties in the CCI Biomass dataset to coarser spatial resolutions, we implement a 301 × 301 kernel (Figure 4-3) representing the spatial autocorrelation from the ensemble model (Figure 4-2) in 2-D. Each pixel of the kernel represents the error correlation $r_{spat,ij}$ between pixel *i*, assumed to be in the centre, and pixel *j* at a certain distance from *i*. The size of the kernel was limited to 301 × 301 pixels (i.e., approximately 30 km × 30 km) as a trade-off between computational efficiency and capturing as many single error correlation values as possible in the computation of the error covariance component of the average AGB. A larger kernel would have captured error correlations below 0.01, which have negligible impact on the covariance term in Equation (3-17).
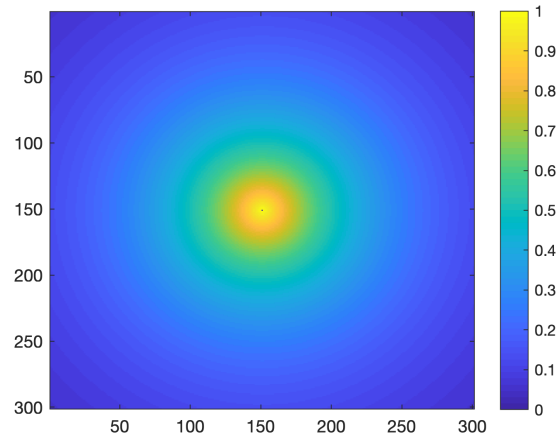
Figure 4-3: Two-dimensional kernel representing the error correlation as a function of lag distance.

To illustrate the result of the averaging procedure implemented to generate an average AGB map from the dataset at its original spatial resolution, we show in Figure 4-4 the average AGB datasets obtained by averaging to 0.01° and 0.5°. The AGB maps become smoother for increasing averaging window while the standard deviation of the average AGB decreases. The strong spatial autocorrelation of the AGB error at the scale of a kilometre implies that the standard error of AGB at 0.01° decreases by only by a small fraction compared to the original resolution; for example, the standard error of tropical rainforest decreased from on average 50% at 100 m to 35% at 1,000 m. At 0.5° spatial resolution, the standard deviation instead was mostly below 15%, except for sparsely vegetated regions.
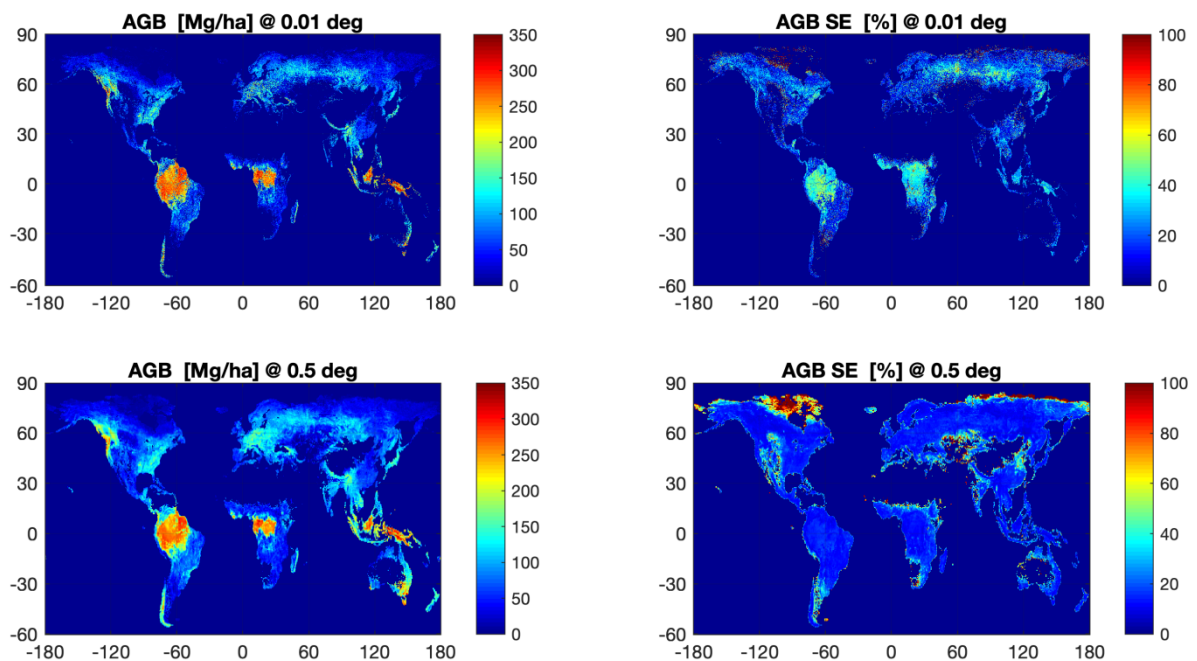


Figure 4-4: Maps of averaged AGB from a CCI Biomass AGB dataset at 0.01° (top left) and 0.5° (bottom left). The corresponding maps of AGB standard error (relative to the AGB value) are displayed in the top right panel (0.01°) and bottom right panel (0.5°).

# 5 Methods to assign precision to AGB change estimates

AGB change is defined as the difference of AGB estimated at two epochs. In the ATBD [RD-3], we described the reasoning behind this definition and the implications concerning the reliability of the AGB changes based on estimates of AGB from different EO datasets. At the full resolution of the AGB maps, the variance of the AGB change $\delta(AGB_{change})^2$ is defined as the sum of the individual variances $\delta(AGB_i)^2$ with i = 1 and 2 being the epoch of the AGB estimate.

$$\delta(AGB_{change})^2 = \delta(AGB_1)^2 + \delta(AGB_2)^2 \qquad (3\text{-}22)$$

Additional terms will appear if a bias correction is applied to each of the AGB estimates. These terms correspond to the standard deviation of the bias estimate for date 1 and date 2. These terms, however, would be applied only at the spatial resolution of the bias maps, i.e., 0.1°, in which case the standard deviation of the two AGB estimates would need to account for the averaging and the spatial correlation of errors (Yang et al., 2020).

# 6 References

Chauhan, N. S., Lang, R. H. and Ranson, K. J. (1991). Radar modeling of a boreal forest. *IEEE Transactions on Geoscience and Remote Sensing,* 29 (4), 627-638.

Dubayah, R.O., A. Swatantran, W. Huang, L. Duncanson, H. Tang, K. Johnson, J.O. Dunne, and G.C. Hurtt. 2017. CMS: LiDAR-derived Biomass, Canopy Height and Cover, Sonoma County, California, 2013. ORNL DAAC, Oak Ridge, Tennessee, USA. https://doi.org/10.3334/ORNLDAAC/1523

Garcia, M., Popescu, S., Riano, D., Zhao, K., Neuenschwander, A., Agca, M. and Chuvieco, E. (2012). Characterization of canopy fuels using ICESAT/GLAS data. *Remote Sensing of Environment,* 123, 81-89.

Hansen, M.C., Potapov, P.V., Moore, R., Hancher, M., Turubanova, S.A., Tyukavina, A., Thau, D., Stehman, S.V., Goetz, S.J., Loveland, T.R., Kommareddy, A., Egorov, A., Chini, L., Justice, C.O., Townshend, J.R.G., 2013. High-resolution global maps of 21-st century forest cover change. Science 342, 850–853. https://doi.org/10.1126/science.1244693

Kurum, M., Lang, R. H., O'Neill, P. E., Joseph, A. T., Jackson, T. J. and Cosh, M. H. (2009). L-Band radar estimation of forest attenuation for active/passive soil moisture inversion. *IEEE Transactions on Geoscience and Remote Sensing,* 47 (9), 3026-3040.

Labriere, N., Tao, S., Chave, J., Scipal, K., Toan, T.L., Abernethy, K., Alonso, A., Barbier, N., Bissiengou, P., Casal, T., Davies, S.J., Ferraz, A., Herault, B., Jaouen, G., Jeffery, K.J., Kenfack, D., Korte, L., Lewis, S.L., Malhi, Y., Memiaghe, H.R., Poulsen, J.R., Rejou-Mechain, M., Villard, L., Vincent, G., White, L.J.T., Saatchi, S., 2018. In Situ Reference Datasets From the TropiSAR and AfriSAR Campaigns in Support of Upcoming Spaceborne Biomass Missions. IEEE J. Sel. Top. Appl. Earth Observations Remote Sensing 11, 3617–3627. https://doi.org/10.1109/JSTARS.2018.2851606

Los, S. O., Rosette, J., Kljun, N., North, P. R. J., Chasmer, L., Suárez, J. C., Hopkinson, C., Hill, R. A., van Gorsel, E., Mahoney, C. and Berni, J. A. J. (2012). Vegetation height and cover fraction between 60° S and 60° N from ICESat GLAS data. *Geoscientific Model Development,* 5, 413-432.

McRoberts, R.E., 2006. A model-based approach to estimating forest area. Remote Sensing of Environment 103, 56–66. https://doi.org/10.1016/j.rse.2006.03.005

Nilsson, M., Nordkvist, K., Jonzén, J., Lindgren, N., Axensten, P., Wallerman, J., Egberth, M., Larsson, S., Nilsson, L., Eriksson, J. and Olsson, H. (2017). A nationwide forest attribute map of Sweden predicted using airborne laser scanning data and field data from the National Forest Inventory. *Remote Sensing of Environment,* 194, 447-454.

Praks, J., Antropov, O. and Hallikainen, M. (2012). LIDAR-aided SAR interferometry studies in boreal forest: Scattering phase center and extinction coefficient at X- and L-band. *Remote Sensing,* 50 (10), 3831-3843.

Santoro, M., Askne, J., Smith, G., Fransson, J.E.S., 2002. Stem volume retrieval in boreal forests from ERS-1/2 interferometry. Remote Sensing of Environment 81, 19–35. https://doi.org/10.1016/S0034-4257(01)00329-7

Santoro, M., Beaudoin, A., Beer, C., Cartus, O., Fransson, J.E.S., Hall, R.J., Pathe, C., Schepaschenko, D., Schmullius, C., Shvidenko, A., Thurner, M., Wegmüller, U., 2015. Forest growing stock volume of the northern hemisphere: Spatially explicit estimates for 2010 derived from Envisat ASAR data. Remote Sensing of Environment 168, 316–334. https://doi.org/10.1016/j.rse.2015.07.005

Santoro, M., Cartus, O., Carvalhais, N., Rozendaal, D., Avitabilie, V., Araza, A., de Bruin, S., Herold, M., Quegan, S., Rodríguez Veiga, P., Balzter, H., Carreiras, J., Schepaschenko, D., Korets, M., Shimada, M., Itoh, T., Moreno Martínez, Á., Cavlovic, J., Cazzolla Gatti, R., da Conceição Bispo, P., Dewnath, N., Labrière, N., Liang, J., Lindsell, J., Mitchard, E.T.A., Morel, A., Pacheco Pascagaza, A.M., Ryan, C.M., Slik, F., Vaglio Laurin, G., Verbeeck, H., Wijaya, A., Willcock, S., 2021. The global forest above-ground biomass pool for 2010 estimated from high-resolution satellite observations. Earth System Science Data 13, 3927–3950. https://doi.org/10.5194/essd-2020-148

Sheen, D. R., Malinas, N. P., Kletzli, D. W., Lewis, T. B. and Roman, J. F. (1994). Foliage transmission measurements using a ground-based ultrawide band (300-1300 MHz) SAR system. *IEEE Transactions on Geoscience and Remote Sensing,* 32 (1), 118-130.

Shinohara, H., Homma, T., Nohmi, H., Hirosawa, H. and Tagawa, T. (1992). Relation between L-band microwave penetration / backscattering characteristics and state of trees. In: *IGARSS'92*. City: IEEE Publications, Piscataway, NJ, 539-541.

Simard, M., Pinto, N., Fisher, J. B. and Baccini, A. (2011). Mapping forest canopy height globally with spaceborne lidar. *Journal of Geophysical Research - Biogeosciences,* 116, G04021.

Ulaby, F. T., Whitt, M. W. and Dobson, M. C. (1990). Measuring the propagation properties of a forest canopy using a polarimetric scatterometer. *IEEE Transactions on Antennas and Propagation,* 38 (2), 251-258.

Yang, H., Ciais, P., Santoro, M., Huang, Y., Li, W., Wang, Y., Bastos, A., Goll, D., Arneth, A., Anthoni, P., Arora, V.K., Friedlingstein, P., Harverd, V., Joetzjer, E., Kautz, M., Lienert, S., Nabel, J.E.M.S., O'Sullivan, M., Sitch, S., Vuichard, N., Wiltshire, A., Zhu, D., (2020). Comparison of forest above-ground biomass from dynamic global vegetation models with spatially explicit remotely sensed observation-based estimates. *Global Change Biology*, 26, 3997–4012. https://doi.org/10.1111/gcb.15117